Travelling-Wave NMR and MRI

David O. Brunner[1], Nicola De Zanche[2], Jürg Fröhlich[3], Jan Paska[4],

Klaas P. Pruessmann[5*]

[1]Institute for Biomedical Engineering, University and ETH Zürich, Gloriastrasse 35,

8092 Zurich, E-mail: brunner@biomed.ee.ethz.ch, Telephone: +41446326179,

Fax: +41 44 632 11 93,

[2]Institute for Biomedical Engineering, University and ETH Zürich,

E-mail: dezanche@ieee.org , Telephone: +1 (780) 989 8155,

[3]Laboratory for Electromagnetic Fields and Microwave Electronics, ETH Zurich,

E-mail: j.froehlich@ifh.ee.ethz.ch, Telephone: +41 44 6324385,

[4]Laboratory for Electromagnetic Fields and Microwave Electronics, ETH Zurich,

E-mail: paska@ifh.ee.ethz.ch, Telephone: +41 44 6320430,

[5]Institute for Biomedical Engineering, University and ETH Zürich, Gloriastrasse 35,

8092 Zürich, E-mail: pruessmann@biomed.ee.ethz.ch, Telephone: +41 44 632 66 96,

Fax: +41 44 632 11 93

In this work we introduce a novel concept of signal excitation and detection to NMR and MRI. We propose to abandon the long-standing principle of near-field inductive coupling between nuclear magnetization and the detector, commonly an RF resonator, by far-range travelling-wave interaction with an antenna probe. Along with the feasibility of this approach we demonstrate that it addresses a key obstacle to high-field MRI in large samples, particularly in humans. We believe that the transition to travelling-wave excitation and detection is significant both from a fundamental, physical point of view and with respect to the numerous applications that NMR and MRI have in the sciences and medicine.

Body text

Nuclear magnetic resonance (NMR)[1, 2] ranks among the most versatile experimental methods in chemistry, physics, and biology[3], providing insight into the structure and dynamics of matter at the molecular scale. Its imaging variant, magnetic resonance imaging (MRI)[4, 5], is widely used to examine the anatomy, physiology, and metabolism of the human body. NMR signal detection is traditionally based on Faraday induction[6] in one or multiple radiofrequency (RF) resonators[7-10] that surround the sample closely for high efficiency. Alternative principles have been explored, involving structured-material flux guides[11], SQUIDs[12], atomic magnetometers[13], Hall probes[14], or magneto-resistive elements[15]. However, all NMR implementations to-date have in common that they rely on intimate coupling between the detector and the object under investigation. Here we show that NMR can also be excited and detected by far-range interaction, relying on travelling RF waves sent and received by an antenna (Fig. 1). One benefit of this approach is more uniform coverage of samples that are larger than the wavelength of the NMR signal. It thus addresses an important current issue in MRI of humans at very high magnetic fields. Allowing a significant distance between the probe and the sample, travelling-wave interaction also introduces new options in the design of NMR experiments and systems.

Uniform spatial coverage in NMR and MRI is traditionally achieved by tailoring the reactive near field of resonant Faraday probes [7-10]. This approach is valid when the RF wavelength at the Larmor frequency is substantially larger than the target volume, which

does not hold for recent wide-bore high-field systems. At the currently highest field strength that is used for human studies, 9.4 tesla[16, 17], the resonance frequency of hydrogen nuclei reaches 400 MHz, corresponding to a wavelength in tissue on the order of 10 cm. At such short wavelengths head or body resonators form standing-wave field patterns, which degrade MRI results by causing regional signal losses and perturbing the contrast between different types of tissue.

The non-uniformity of standing waves is due to the underlying electrodynamics, which require that the magnetic field exhibit curvature according to its frequency and the ambient material. Standing waves fulfill this condition by spatial variation of the field magnitude (Fig. 1a). However the required field curvature can also be translated, partly or wholly, into phase variation. Causing the underlying field pattern to propagate through space such phase variation reduces the variation of the field magnitude. Notably, the limiting case of a plane wave exhibits perfectly uniform magnitude at any wavelength. In addition, travelling RF waves offer a natural means of exciting and detecting NMR across large distances (Fig. 1b).

Despite these attractive features travelling-wave NMR has not been explored so far. In traditional cylindrical setups the formation of travelling waves at the NMR frequency is suppressed by structures surrounding the sample, such as gradient coils, cryostats, and RF screens. Their conductive surfaces admit axially travelling waves only beyond some cut-off frequency which is roughly reciprocal to the bore width. Therefore travelling-wave

NMR requires a high-field magnet that also has a wide bore in order to bring the cut-off frequency below the NMR frequency.

To fulfill this requirement we used a cylindrical, superconducting 7.0-tesla magnet with a 58 cm-diameter bore lined with an RF screen (Fig. 1c). The screen was made from a steel mesh designed to provide high conductance at RF frequencies while blocking audio-frequency eddy currents induced by the surrounding gradient coils. When enclosing only air the bore has a cut-off frequency of 303 MHz, which is still just above the proton Larmor frequency of 298 MHz. However, the frequency limit is reduced when dielectric material is brought into the bore. Even small amounts of dielectric loading enable the formation of axially travelling waves at the NMR frequency, effectively using the RF screen as a waveguide. A human body in particular — containing large amounts of water, which is a strong dielectric — reduces the cut-off frequency sufficiently to clearly enter the travelling-wave regime.

NMR via such travelling waves requires a new type of probe. Instead of the reactive near field of the sample a travelling-wave probe must couple to the propagating modes of the waveguide. To do so it no longer needs to be close to the sample but can be placed anywhere along the bore. Requirements of this sort are well known in microwave engineering and can be addressed by a range of technical solutions. For the present work the NMR probe was implemented in the form of a circularly polarized patch antenna[18] (Fig. 1c).

Using this setup the principle of travelling-wave NMR was first demonstrated by spectroscopy of an aqueous 10% ethanol solution. Proton NMR was excited and detected by the patch antenna, which was initially mounted at the end of the RF screen, 70 cm from the sample. The resulting spectrum (Fig. 2a) shows the expected dominant water peak as well as the methyl and methylene resonances of the ethanol molecule. The experiment was then repeated with gradually increasing antenna distances. As the magnified methyl triplets in Fig. 2b show, consistent spectrum quality was obtained with the probe placed well outside the magnet and a well-resolved spectrum was still detected at a distance of 2.6 m from the sample. The evident loss of sensitivity at large distance reflects the expected decrease in coupling between the antenna and the modes of the bore. Higher sensitivity at large distances would be achieved with an antenna of greater directivity or a longer waveguide.

The spatial uniformity of the travelling waves was studied in an extended sample of 50 cm in length, formed by two adjacent bottles filled with mineral oil. At first this arrangement did not yield fully uniform RF coverage yet, as illustrated by the imaging results shown in Fig. 3a. The residual non-uniformity indicates the presence of a standing RF wave superimposed on the intended travelling component. It is caused mainly by slight reflections at the transitions between the bottles and the empty sections of the bore, which entail changes in wave impedance. The reflections can be mitigated by wave-impedance matching and additional loading. To demonstrate this two further bottles were added at the far end of the sample, the second one containing a conductive water solution to act as a termination dissipating incident wave energy. This modification indeed

rendered the MRI results substantially more uniform, indicating the presence of almost purely travelling RF waves (Fig. 3b).

For reasons of safety, initial in-vivo experiments targeted only a volunteer's lower extremities ensuring that the chest and head remained outside the waveguide. The antenna was placed at the opposite end of the bore, 70 cm from the ankle. The resulting magnetic-resonance image (Fig. 4a) shows the right lower leg with good uniformity over a large volume. The field of view of 50 cm is the maximum possible with the gradient system used and is not limited by the travelling-wave concept. Wave-impedance matching was not necessary in this case because the leg per se forms a sufficiently smooth, tapered impedance transition. For comparison the same imaging procedure was repeated with a commercially available birdcage resonator optimized for head MRI at 7 tesla. The result thus obtained (Fig. 4b) exhibits smaller coverage, reflecting inherent limitations of resonant probes. The standing-wave nature of its rung currents limits the feasible length of the birdcage probe, which is 17 cm for this model. On longer rungs the RF current would exhibit an even more non-uniform distribution[19], equally causing an axial sensitivity drop-off and rendering the resonator unstable[20].

While it was possible to cover the lower legs uniformly, significant RF attenuation is expected to occur along the full length of a human body. Simulations of the setup in Fig. 1c, assuming an adult male subject, indicate that in total the body absorbs approximately 90% of the RF power coupled into the waveguide and only the remaining 10% are radiated off its far end. Less attenuation is expected for shorter or slimmer

persons or when using an even wider bore. Based on the same simulations the coupling efficiency of the patch antenna was estimated at 80%, a value that can certainly be improved by optimizing the strategy of driving the waveguide modes.

Besides coverage and uniformity the travelling-wave concept will also affect the sensitivity and RF power efficiency of NMR experiments. According to the reciprocity of NMR signals[21] the sensitivity of an RF probe is closely related to its efficiency, i.e., its yield of circularly polarized RF magnetic field at reference input power. Resonant near-field probes achieve high efficiency by concentrating RF energy and dissipation in the sample and the probe itself. By contrast, the travelling-wave approach relies on RF energy flowing through the setup, requiring that part of it be absorbed beyond the target volume. This can be done by a dedicated absorber device or diffusely outside the waveguide as was the case in our initial experiments. With either solution the necessary absorber losses will take some toll in terms of efficiency and sensitivity, constituting a drawback of travelling-wave probes compared with resonators.

Reduced probe efficiency is the lesser concern because it can be addressed by using higher driving power. In-vivo MRI is usually not limited by technical RF power constraints but rather by sample heating, to which the absorber losses do not contribute. The corresponding sensitivity loss, caused by thermal noise originating from any material that absorbs RF power during transmission, is more limiting. One potential way of avoiding it is to use a dedicated absorber structure at low or cryogenic temperature. For MRI applications it is also conceivable to combine travelling-wave excitation with local

detection by an array of detunable surface resonators[9]. Such a hybrid approach will reconcile the improved coverage and safety advantage of travelling-wave excitation with the sensitivity benefit of close-range array detection.

With respect to net sensitivity another potential concern is the phase delay that results from signal propagation to and from the resonant nuclei. For large samples it will give rise to significant phase differences between signals travelling different distances, as illustrated experimentally in the online supporting material. MRI will not be hampered by this effect as long as the spatial variation of the RF phase is resolved by the imaging process. However spectroscopic experiments could suffer from delay-related dephasing. To address this problem the antenna pair should generally be designed and positioned such that the total phase delay is the same across the volume of interest. In a uniform waveguide this can be readily achieved by using separate transmitting and receiving antennas on opposite sides of the sample. Alternatively, a gradient encoding blip could be applied between excitation and reception to compensate for variable phase delay, effectively refocusing the spin radiation for reception by the transmitter antenna

Entering the far-field realm, travelling-wave NMR prompts analogies with electron spin resonance[22] and nonlinear optics[23]. Adopting principles and devices from these fields may enable studying phenomena analogous to, e.g., photon echoes[24], four-wave mixing[25], and self-induced transparency[26]. Potentially useful analogies can also be drawn with the large variety of more widespread technologies that rely on travelling-wave phenomena, including manifold imaging modalities, radar, and telecommunication. In the present

work, the established concepts of waveguides and antennas have already proven useful. Clearly, by adopting propagating waves NMR also incurs known complications of this realm, such as material-dependent diffraction and attenuation. These effects will likely be encountered, e.g., in MRI of the human torso, exhibiting pronounced dielectric interfaces such as the shoulders and the diaphragm. An initial experimental illustration of dielectric effects in a torso phantom is given in the supporting online material. However, travelling-wave MRI may equally rely on established means of countering such problems. One example is wave-impedance matching, which has been demonstrated here in a basic form. Analogously to index matching in microwave and optical technology, wave-impedance matching can be achieved using a wide range of distributions of dielectric, magnetically permeable, or conductive material and thus offers great inherent freedom for tailoring resulting RF field distributions.

By improving the extent and uniformity of spatial coverage travelling-wave MRI promises to facilitate exploring the benefits of the currently highest field strengths for human studies. A further promising area of application is high-field screening. The ability to perform spatially resolved NMR efficiently in a large volume will facilitate studying large numbers of small animals[27] or inanimate samples in parallel. Finally, introducing a significant distance between the sample and the NMR probe has multiple beneficial side-effects. In such a configuration the probe is not loaded by losses in the sample, which simplifies impedance matching and renders the probe performance substantially more robust than that of near-field high-frequency probes. This situation also simplifies safety considerations in human studies by avoiding exposure to strong short-range electric fields

emanating from the probe. Furthermore, placing the probe far away frees up space in the center of costly high-field magnets, may improve the comfort of human subjects and facilitates bringing in alternative equipment, such as stimulation devices for studies of brain function.

Methods summary

All experiments were performed using a 7-tesla human whole-body MRI system (Philips Healthcare, Cleveland, Ohio). The cylindrical RF screen forming the waveguide (diameter = 580 mm) was made from a stainless-steel mesh. The safety of the in-vivo experiments was ensured by a built-in monitoring unit limiting the RF power output to an average of 10 W, i.e., the same value as used for the commercial volume resonator. The patch antenna[18] consisted of a thin copper disk and a backplane, each on a PMMA former, and is tuned by adjusting an air-filled gap. The antenna was driven in quadrature through TTL-controlled T/R switches.

The spectra shown in Fig. 2 were obtained using a stimulated-echo sequence (STEAM) for volume selection. The sample was a 10% aqueous ethanol solution in a 1-litre glass beaker and was axially tapered by bottles filled with distilled water. The data shown in Fig. 3 were aquired with a 2D gradient-echo sequence. Low flip angles were used in order to faithfully represent the RF field distribution. The bottles were filled with 3 litres each of Marcol 82 mineral oil. The in-vivo data of Fig. 4 were acquired using a low-flip-angle 3D gradient-echo sequence with identical sequence parameters for both scans. Only the RF power was reduced to about 25% in the resonator scan to implement similar flip angles in the center. The transfer and attenuation of RF power were estimated by finite-

difference time-domain (FDTD) simulation incorporating the antenna, the waveguide and a detailed anatomical model of an adult male human[28].

Acknowledgements

We thank Dr. Nico van den Berg for stimulating and clarifying discussions.

Author information:

The authors have no financial interests to disclose.

Correspondence and requests for materials should be addressed to: K.P.P.

References

1. Bloch, F., Hansen, W. W. & Packard, M. The Nuclear Induction Experiment. *Phys Rev* **70**, 474 (1946).
2. Purcell, E. M., Torrey, H. C. & Pound, R. V. Resonance Absorption by Nuclear Magnetic Moments in a Solid. *Phys Rev* **69**, 37 (1946).
3. de Graaf, R. A. *NMR Spectroscopy* (John Wiley & Sons Ltd, West Sussex, England, 2007).
4. Lauterbur, P. C. Image Formation by Induced Local Interactions: Examples Employing Nuclear Magnetic Resonance. *Nature* **242**, 190-197 (1973).
5. Kumar, A., Welti, D. & Ernst, R. R. NMR Fourier Zeugmatography. *J Magn Reson* **18**, 69-83 (1975).
6. Hahn, E. L. Nuclear Induction Due to Free Larmor Precession. *Phys Rev* **77**, 297 (1950).
7. Hayes, C. E., Edelstein, W. A., Schenk, J. F., Mueller, O. M. & Eash, M. An efficient, highly homogeneous radiofrequency coil for whole-body NMR imaging at 1.5 T. *J Magn Reson* **63**, 622-628 (1985).
8. Tropp, J. Theory of the birdcage resonator. *J Magn Reson* **82**, 51-62 (1989).
9. Roemer, P. B., Edelstein, W. A., Hayes, C. E., Souza, S. P. & Mueller, O. M. The NMR phased array. *Mag Reson Med* **16**, 192-225 (1990).
10. Vaughan, J. T., Hetherington, H. P., Otu, J. O., Pan, J. W. & Pohost, G. M. High frequency volume coils for clinical NMR imaging and spectroscopy. *Magn Reson Med* **32**, 206-218 (1994).

11. Wiltshire, M. C. K. et al. Microstructured Magnetic Materials for RF Flux Guides in Magnetic Resonance Imaging. *Science* **291**, 849-851 (2001).

12. Day, E. P. Detection of NMR Using a Josephson-Junction Magnetometer. *Phys Rev Lett* **29**, 540 (1972).

13. Savukov, I. M. & Romalis, M. V. NMR Detection with an Atomic Magnetometer. *Phys Rev Lett* **94**, 123001 (2005).

14. Boero, G., Besse, P.-A. & Popovic, R. Hall detection of magnetic resonance. *APL* **79**, 1498-1501 (2001).

15. Verpillat, F. et al. Remote detection of nuclear magnetic resonance with an anisotropic magnetoresistive sensor. *PNAS* **105**, 2271–2273 (2008).

16. Vaughan, T. et al. 9.4T human MRI: Preliminary results. *Magn Reson Med* **56**, 1274-1282 (2006).

17. Atkinson, I. C., Renteria, L., Burd, H., Pliskin, N. H. & Thulborn, K. R. Safety of Human MRI at Static Fields Above the FDA 8T Guideline: Sodium Imaging at 9.4T Does Not Affect Vital Signs or Cognitive Ability. *J Magn Reson Imag* **26**, 1222-1227 (2007).

18. Balanis, C. A. *Antenna Theory: Analysis and Design* (John Wiley &Sons, New York, 2005).

19. Bogdanov, G. & Ludwig, R. Coupled microstrip line transverse electromagnetic resonator model for high-field magnetic resonance imaging. *Magn Reson Med* **47**, 579-593 (2002).

20. Harpen, M. D. Cylindrical coils near self-resonance. *Magn Reson Med* **30**, 489-493 (1993).

21. Hoult, D. I. The principle of reciprocity in signal strength calculations: a mathematical guide. *Conc Magn Reson* **12**, 173–187 (2000).

22. Gulla, A. F. & Budil, D. E. Engineering and Design Concepts for Quasioptical High-Field Electron Paramagnetic Resonance. *Conc Magn Reson B* **22B**, 15–36 (2004).

23. Boyd, R. W. *Nonlinear Optics* (Elsevier Science, San Diego, 2003).

24. Kurnit, N. A., Abella, I. D. & Hartmann, S. R. Observation of a Photon Echo. *Phys Rev Lett* **13**, 567 (1964).

25. Armstrong, J. A., Bloembergen, N., Ducuing, J. & Pershan, P. S. Light Waves at the Boundary of Nonlinear Media. *Phys Rev* **128**, 606 (1962).

26. McCall, S. L. & Hahn, E. L. Self-Induced Transperancy. *Phys Rev* **183**, 457-490 (1969).

27. Bock, N. A., Konyer, N. B. & Henkelman, R. M. Multiple-mouse MRI. *Magn Reson Med* **49**, 158-167 (2003).

28. Christ, A. et al. in European BioElectromagnetics Association (Bordeaux, France, 2007).

Figure Legends

Figure 1: Working principles of traditional and travelling-wave NMR. a) Traditional resonant probes form a standing RF wave within the sample. Its magnetic component B causes nutation of the nuclear magnetization M and governs the probe's sensitivity in the receiving mode. b) In the novel approach an antenna probe interacts with the sample via a travelling wave. c) In a cylindrical high-field magnet travelling waves at the NMR frequency can be supported by lining the bore with an RF waveguide. NMR in the sample can then be excited and detected remotely by placing the antenna at the end of the magnet.

Figure 2: Demonstration of travelling-wave NMR in an aqueous 10% ethanol solution. a) NMR spectrum obtained at an antenna distance of 70 cm, showing water (1), methylene (2), and methyl (3) resonances. b) Details of the methyl triplet as observed with increasing distance.

Figure 3: Example of wave-impedance matching in travelling-wave MRI: a) Non-uniform coverage of two phantom bottles is caused by residual standing RF waves, which can be suppressed by b) wave-impedance matching and dissipation in a termination load.

Figure 4: In vivo results: a) Travelling-wave MRI of a human lower leg in-vivo. b) Identical scan performed with a traditional resonant probe.

Figure S1: Schematic of the patch antenna.

Figure S2: Coverage of very large samples. a) A 2 m long cylinder (7 cm diameter) filled with water was placed concentrically along the wave guide. The gradient-echo image with a field of view of 50 cm shows uniform coverage by the patch antenna. The graph below shows the delay-related progression of the image phase along the line indicated. In these data the phase effect of static field inhomogeneity was corrected for on the basis of two signals obtained with different echo times. Two antennas (1&2) were used, one at each end of the waveguide. In two successive experiments each antenna was used once for transmission while always using both for signal detection. As the plots show, sending and receiving with the same antenna gives rise to a linear phase progression along the phantom (1→1, 2→2). When sending and receiving on opposite sides of the waveguide (1→2, 2→1), the phase progression vanishes due to invariant total phase delay.
b) Image of a large phantom with dimensions similar to a human torso (ASTM phantom), filled with 40 litres of gelled water with conductivity similar to in-vivo tissue. At the bottom the phantom exhibits a narrower extension mimicking the head and extending beyond the field of view covered by the gradient system. The image was obtained by excitation and detection with one patch antenna placed at the end of the waveguide. It can be seen that the dielectric boundaries formed by the top of the head and the shoulders introduce perturbations, which diminish towards the lower regions of the phantom.

Methods

All experiments were performed in a cylindrical superconducting 7.0-tesla magnet (Philips Healthcare, Cleveland, Ohio), equipped with a three-axis gradient system and lined with an RF screen of 58 cm in diameter and 135 cm in length. NMR and MRI data acquisition was performed with an integrated console and spectrometer (Achieva, Philips Healthcare). Throughout, the RF transmitter power was limited to the same values as for human head exposure with a local resonator, i.e. 10 W average forward power and 1.4 kW peak power.

The custom-designed patch antenna is shown in the Supplementary Information (Fig. S1). Its front plane is a 350-mm diameter disk made of copper sheet glued onto a 25 mm-thick acrylic (PMMA) former. The backplane is formed by a square copper sheet mounted on 5 mm acrylic. Acrylic yields negligible proton NMR signal at the echo times used in this work. A variable gap between the two planes was used to tune the antenna to the proton NMR frequency of 298 MHz. The antenna was driven at two points in the front plane forming a right angle with the center of the disk. The radial positions of the feed points were chosen such as to match the impedance of the 50 Ω feed line. To produce circular polarization in the transmission mode the two ports were fed through a 90° hybrid splitter. In receive operation the two channels were connected to independent receive lines of the spectrometer and combined digitally. Switching between transmit and receive operation was performed by TTL-controlled diode switches.

The spectra shown in Fig. 2 were obtained from a 10% solution of ethanol in water, contained in a 1-litre glass beaker. To support the formation of axially travelling waves bottles of distilled water were added on either side of the beaker as dielectric loads. NMR spectra were acquired with a localized STEAM sequence (stimulated echo acquisition mode) with an echo time of 11 ms and a repetition time of 3 s. Low-flip-angle RF pulses were used such that the selected volume of 9 cm^3 changed negligibly with the RF amplitude. The acquisition bandwidth was 2 kHz and 16 phase cycles were performed to cancel spurious echoes. When changing the position of the RF probe all console and spectrometer settings were kept constant.

The data shown in Fig. 3 were obtained from bottles filled with Marcol 82 mineral oil, using a gradient-echo sequence with an echo time of 2.9 ms, a repetition time of 42 ms, and a bandwidth per pixel of 338 Hz. A very small flip angle was chosen to ensure that the image intensity depends linearly on the transmit and receive sensitivity of the probe.

The in-vivo images of a volunteer's right foot (Fig. 4) were acquired with a 3D gradient-echo sequence, yielding an isotropic resolution of 1 mm in 6 minutes. The echo time was 3.1 ms, the repetition time was 12 ms, and the bandwidth per pixel was 376 Hz. All sequence parameters were kept the same for the two probes, except for the transmit power, which was reduced to 25% for the resonator to obtain similar flip angles in the center. The axial length of the field of view of 500 mm was again limited by the gradient system. The resonant probe was a commercially available birdcage resonator with a

diameter of 30 cm and a length of 17 cm (Nova Medical Inc., Wilmington, MA). Both feet resided within the resonator to keep the volunteer in the same position.

Electromagnetic simulations of the in-vivo setup were performed using the finite difference time domain (FDTD) technique (SEMCAD®, Schmid&Partner Engineering AG). The cylindrical RF screen was modeled as a perfect electrical conductor and an anatomical model of an adult male[28], featuring in-vivo dielectric tissue properties, was positioned at its center. The patch antenna was placed equally as in the in-vivo experiment, i.e., at a distance of 70 cm from the ankle. The flow of RF energy through the waveguide was assessed by integrating the Poynting vector over transverse control planes. A first control plane between the antenna and the human served to determine the power coupled into the waveguide. A second one in the loss-free region close to the end of the waveguide was used to calculate the power that is radiated off the far end of the waveguide. The power difference was validated by volume integration of ohmic losses over the entire body.

1

Travelling-wave NMR and MRI

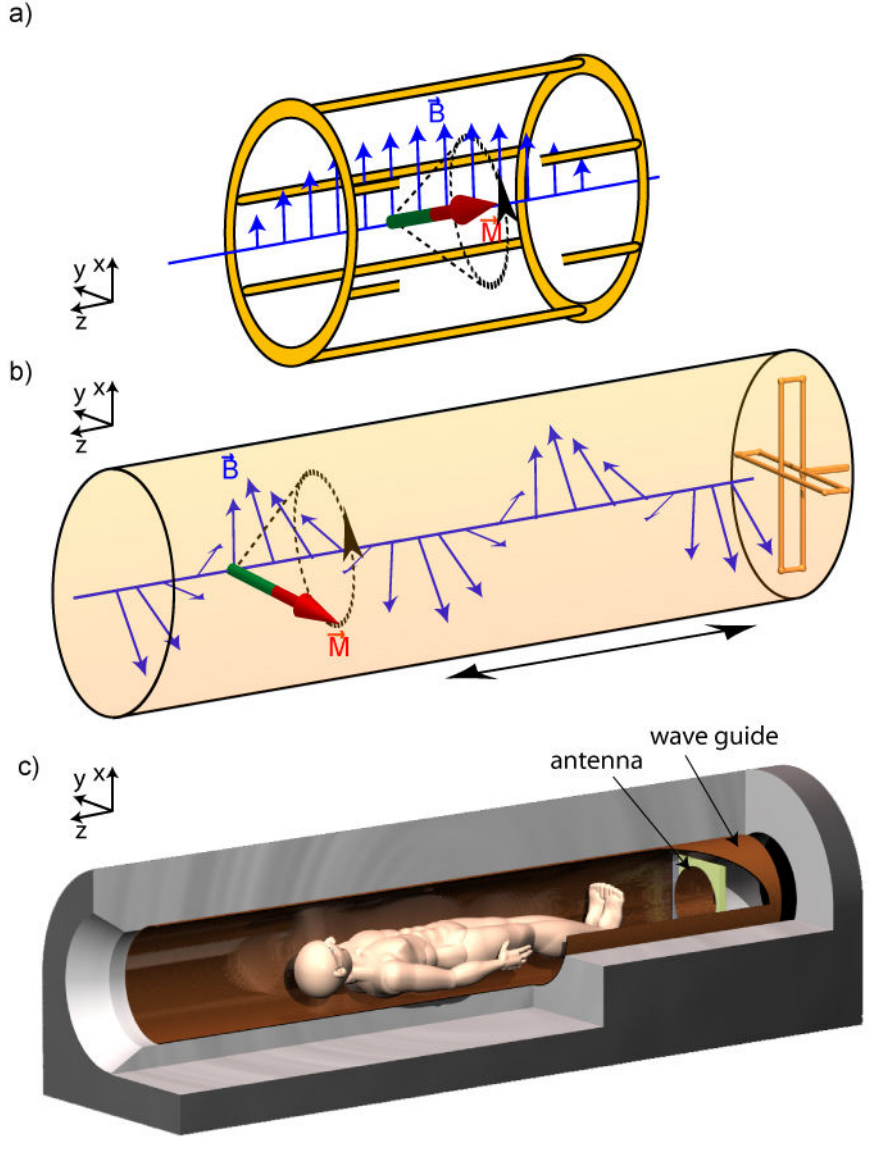
a)
B
M
y x
z
b)
y x
z
B
M
c)
y x
z
antenna
wave guide

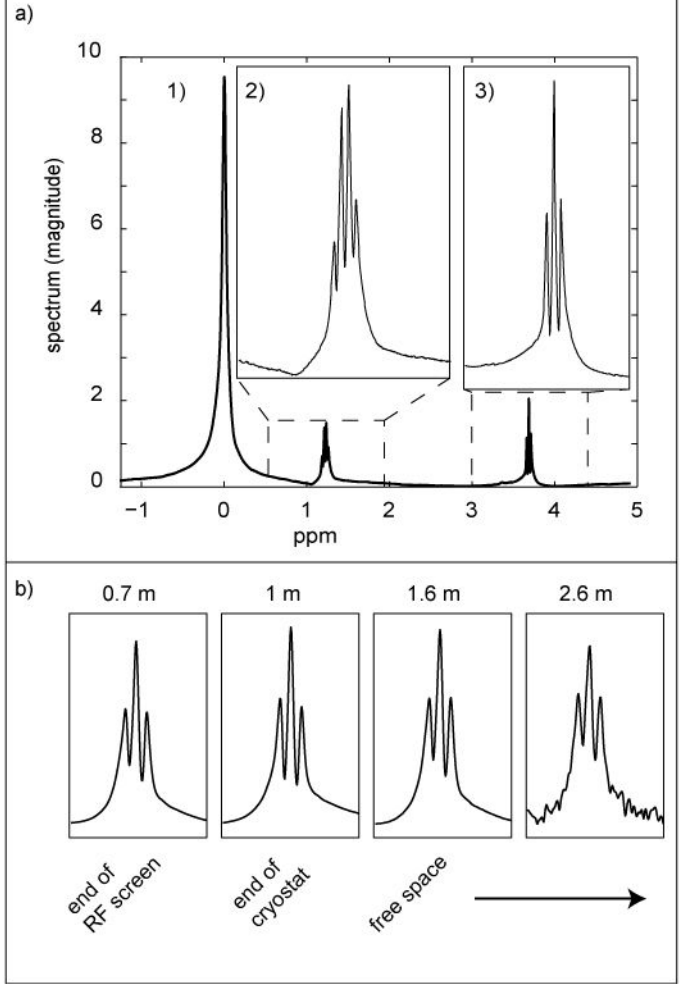
a)
spectrum (magnitude)
ppm
1)
2)
3)
b)
0.7 m
1 m
1.6 m
2.6 m
end of RF screen
end of cryostat
free space

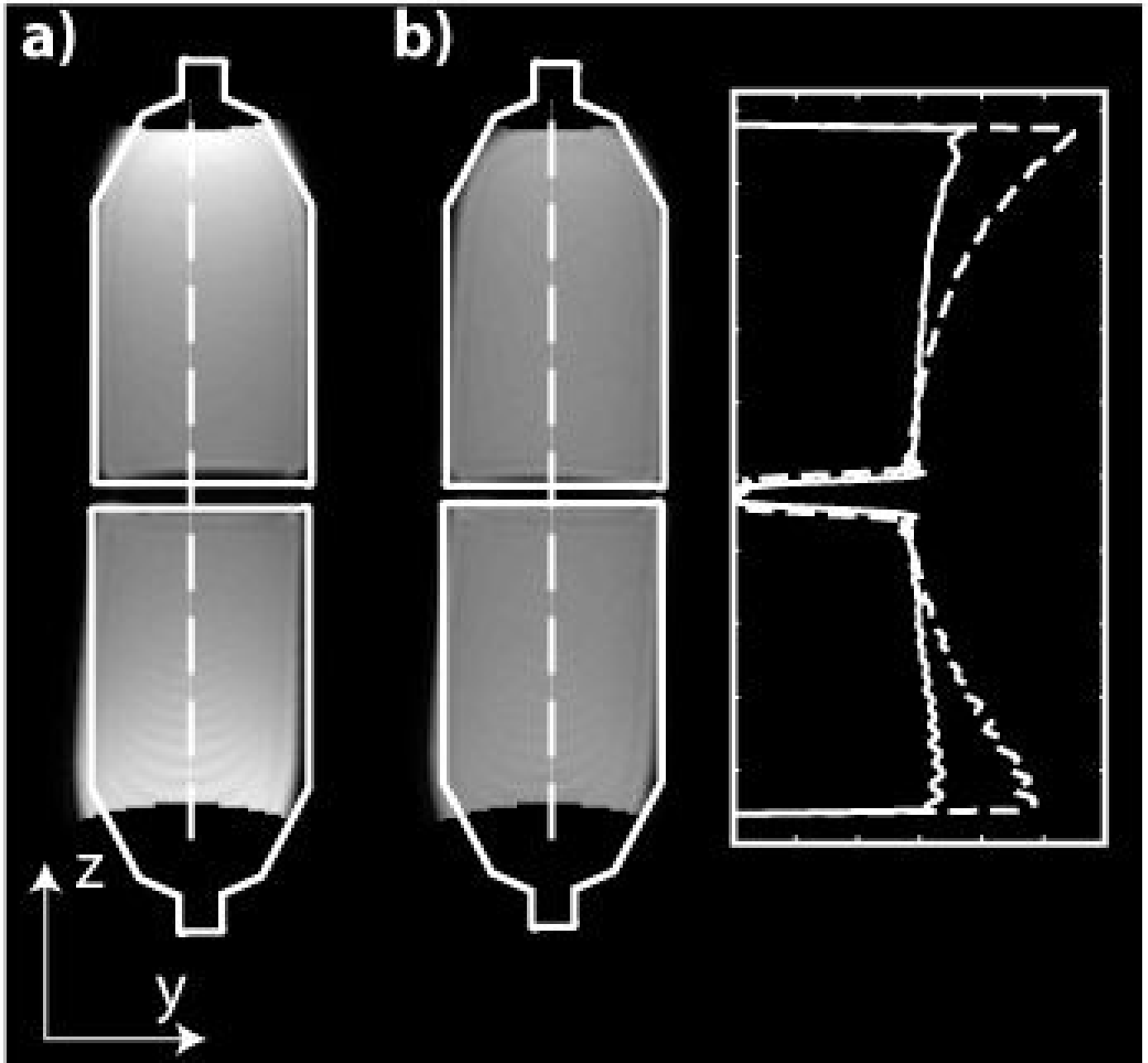
a)
b)
z
y


a)
b)
z
x
500 mm
z
x

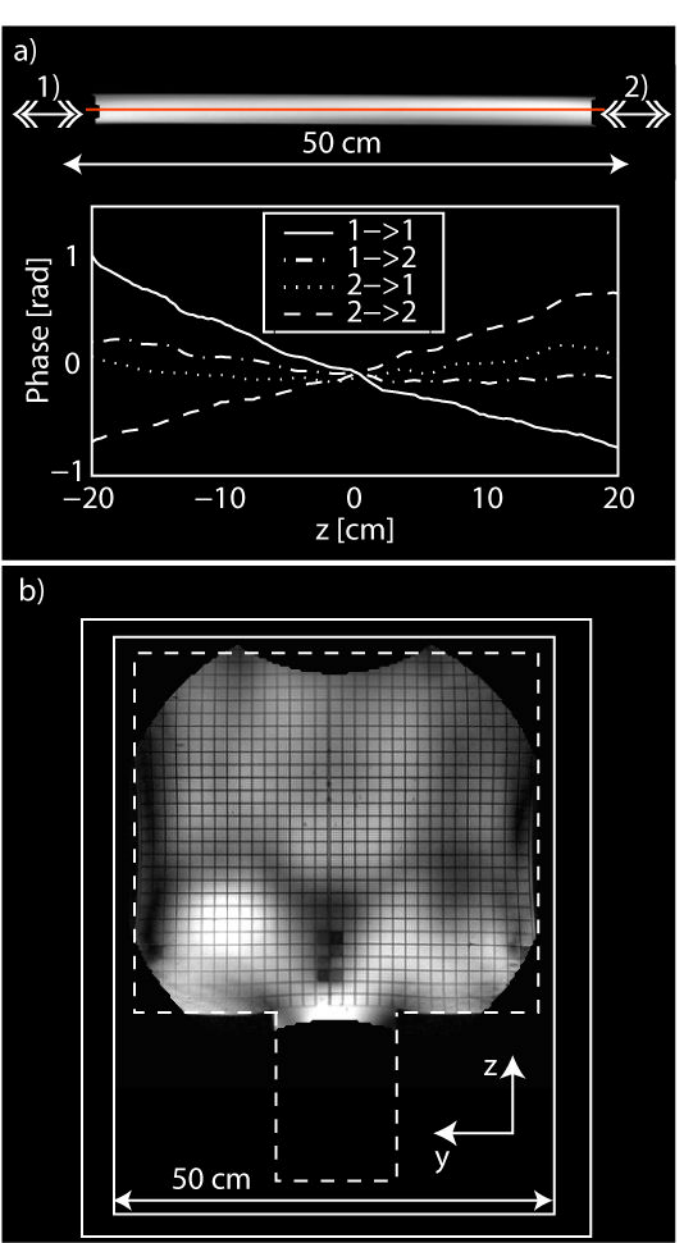
a)
1)
2)
50 cm
1–>1
1–>2
2–>1
2–>2
Phase [rad]
1
0
−1
−20
−10
0
10
20
z [cm]
b)
z
y
50 cm

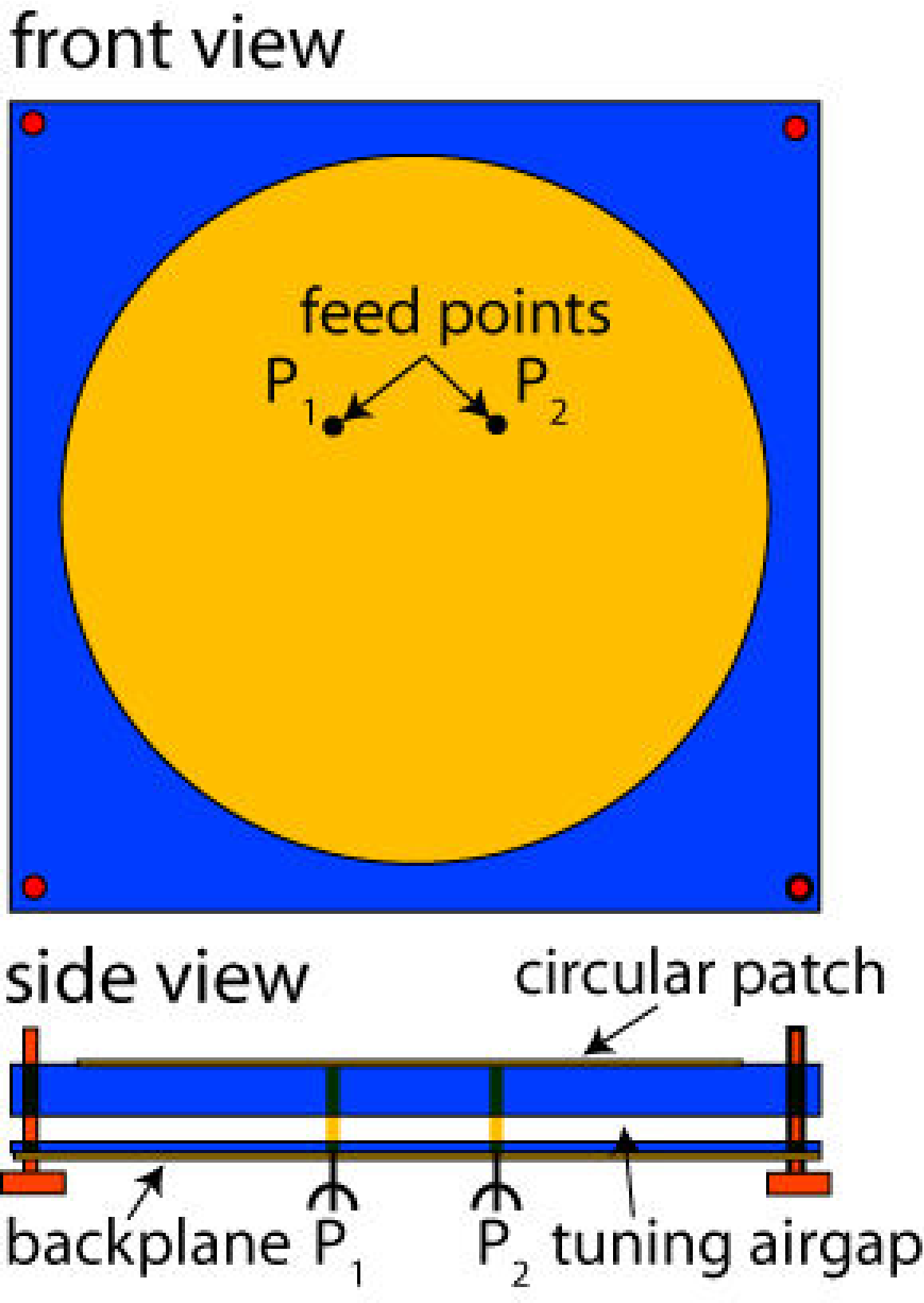
front view
feed points
P1
P2
side view
circular patch
backplane
P1
P2
tuning airgap